stellarator news

**Published by Fusion Energy Division, Oak Ridge National Laboratory**
**Building 9201-2 P.O. Box 2009 Oak Ridge, TN 37831-8071, USA**

Editor: James A. Rome Issue 53 September 1997
E-Mail: jar@ornl.gov Phone (423) 574-1306 Fax: (423) 241-6211
On the Web at *http://www.ornl.gov/fed/stelnews*

# Construction of the LHD plasma vacuum vessel

Construction of the vacuum vessel for the Large Helical Device (LHD) is almost complete. The vacuum vessel, which is made of 15-mm-thick stainless steel, has a major radius of 3900 mm and a minor radius of 1600 mm. Because of the two grooves (each about 1000 mm wide) provided for the helical coils, the vacuum vessel has a dumbbell-shaped cross section.

To facilitate assembly with the helical coils, which were completed earlier (see *Stellarator News* 50), the vacuum vessel was fabricated in sections of two kinds: half-sector units, corresponding to the spherical ends of the dumbbell, and undercoil sections, corresponding to the grip of the dumbbell. The 20 half-sector units, each covered with 80 K thermal shielding plates as shown in Fig. 1, were assembled and installed between the helical coils. They were supported by a winding core that also fixed the position of the helical coils. This assembly of helical coils, half-sector units, and winding core (see Fig. 2) was then placed on the supporting structure and welded to it. After the winding core was removed, the undercoil sections of the vacuum vessel were installed as shown in Fig. 3.

The vacuum vessel has five types of ports. Upper and lower ports (1060 mm × 1730 mm) are used for cooling water feeds, ion cyclotron resonant frequency (ICRF) and electron cyclotron heating, gas puffing, far-infrared interferometer, etc. Outer horizontal ports (2000 mm diam) and inner horizontal ports (700 mm × 480 mm) are used for ICRF heating, local island divertor (LID), Thomson scattering, heavy-ion beam probes, spectroscopy, and other diagnostics. Tangential ports (940 mm diam) are used for neutral beam injection and diagnostics. Ports and flanges will be assembled before the leak test.

The production of steady-state plasmas with durations exceeding 3600 s and a total input power $Q$ of 3 MW is planned for LHD. It is assumed that half of this power will eventually be carried to the divertor plates by the particle flux, while the other half will be carried to the wall of the

## *In this issue . . .*

**Fig. 1.** A half-sector unit covered with 80 K thermal shielding plates.

vacuum vessel by radiation from the plasma. Thus, the vacuum vessel is designed to remove heat from the plasma and to protect the superconducting coils, in addition to providing good vacuum conditions. The temperature of the vacuum vessel must be less than 343 K to limit the temperature of the thermal shielding plates, which are located on the coil side of the vacuum vessel, to 80 K. These plates are made of stainless steel and are supported from the vacuum vessel with 5180 glass-fiber-reinforced plastic (GFRP) legs. The water feeds for wall cooling, which are located on the plasma side of the vacuum vessel, have a U-shaped cross section (10 mm $\times$ 28 mm, 2 mm thick) and are welded to the vacuum vessel wall. Welding an open U-shaped channel to the surface gives better heat conductivity than can be achieved by heavy welding of a normal pipe because the pipe would break

Noriyuki Inoue and Akio Komori for the LHD team
National Institute for Fusion Science
Oroshi-cho, Toki 509-52, Japan
E-mail: inoue@LHD.nifs.ac.jp

**Fig. 2.** The LHD vacuum vessel, with the 20 half sector units were installed between the helical coils on the winding core.

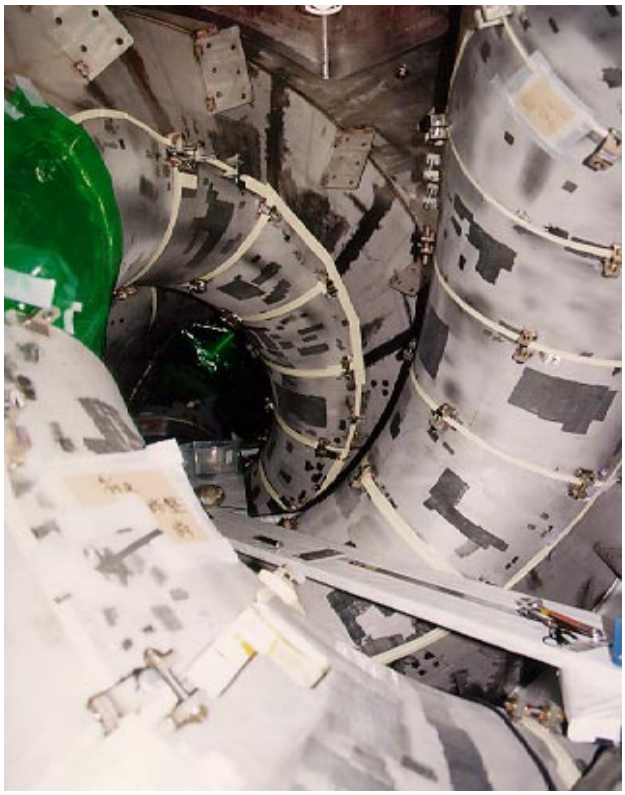

**Fig. 3.** Interior of the LHD vacuum vessel, showing the undercoil parts of the vacuum vessel (corresponding to the grip of the dumbbell-shape cross section).

# Review of 3-D equilibrium calculations for W7-AS

## Part 1: NEMEC-based equilibrium reconstructions

### *Introduction*

Accurate knowledge of the three-dimensional (3-D) structure of the plasma equilibrium is a prerequisite for experiments in stellarators and for the interpretation of experimental data from quite different diagnostics. Therefore, since the calculation of equilibria consistent with the experimental data is an important task, we review here the calculations done for Wendelstein 7-AS (W7-AS) using the 3-D free-boundary code NEMEC [1] with special applications to high beta and to large net toroidal currents in the case of stellarator-tokamak hybrid operation. In the second part of this article (to be published in the next issue), we will present a novel method for fast equilibrium reconstruction for stellarators based on function parameterization.

Although the geometry of the flux surfaces of a stellarator is largely determined by the external coil system, the plasma current densities induced by finite beta, or by internal or external current drive (bootstrap, Okhawa, ohmic and electron cyclotron driven currents) may lead to considerable changes in the equilibrium fields.

To calculate 3-D magnetohydrodynamic (MHD) equilibria with a free boundary, we use the NEMEC code [1] assuming nested flux surfaces. The input consists of profiles for pressure and toroidal current, an estimate of the magnetic axis position and of the plasma boundary, and the vacuum magnetic field. Based on an energy principle, the equilibrium is determined iteratively using a conjugate gradient method. Equilibrium quantities such as flux surface geometry and magnetic field are given in Fourier series with respect to the cylindrical toroidal angle and a poloidal angle coordinate on a radial grid.

An equilibrium reconstruction of a discharge at a given time (assuming stationary conditions, no current diffusion) clearly implies an iterative process of adjusting the input parameters in such way that the resulting equilibrium data best match the experimental information.

### *Beta effects*

Usually, the pressure- induced current densities dominate the changes in the magnetic configuration in discharges with no net toroidal current. The reduced average toroidal curvature of W7-AS leads to smaller Pfirsch-Schlüter (P-S) currents and reduces the Shafranov shift by a factor of 2 when compared to a conventional stellarator. Nevertheless, depending on beta the remaining P-S currents may give rise to appreciable Shafranov shifts, changes in the rotational transform ($\iota$) profile, and a displacement of the plasma as a whole in the accessible $\iota$ range of W7-AS ($0.25 < \iota_{vac} < 0.7$) as shown in Fig. 1. To compensate for the shift in the high-beta phase of the discharge, the vacuum configuration is shifted significantly inward by a vertical field. Thus, the plasma boundary is determined by the inner limiters and the plasma volume becomes a strong function of beta. Therefore, the determination of the volume-averaged beta value $\langle\beta\rangle$is not straightforward but requires equilibrium calculations usually based on kinetic data ($T_e$ and $n_e$ from Thomson scattering data, one time point per shot at the moment, and $T_i = T_e$ for high beta). Using the DIAGNO package [2] to calculate the response in the diamagnetic coil, we can assess the magnetic data again and construct a previously un available time trace of $\langle\beta\rangle$. This is shown in Fig. 2 for some high-beta discharges of the campaign described in *Stellarator News* 46. The good agreement of the NEMEC calculations with experimental data, especially the soft X-ray emissivity, for the high-beta cases was also shown in that article (see the references therein and Ref. [3]).

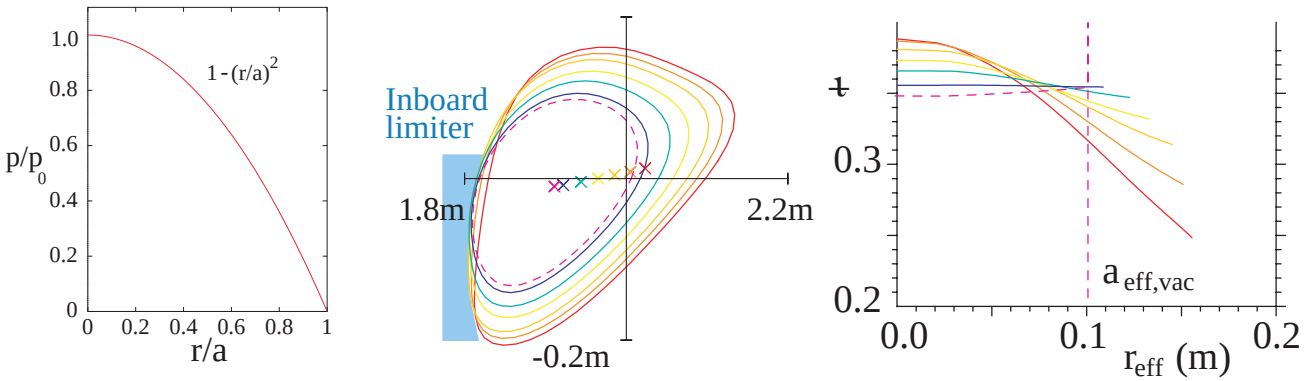


**Fig. 1.** Changes in axis position (x), plasma volume, and $\iota$ profile for a sequence of free-boundary equilibria with $\beta_0$ = 0, 0.3, 1.0, 1.7, 2.4, 3.2 and 4% (dashed lines: vacuum). The vertical dashed line indicates the effective plasma radius $a_{eff}$ of the vacuum configuration.

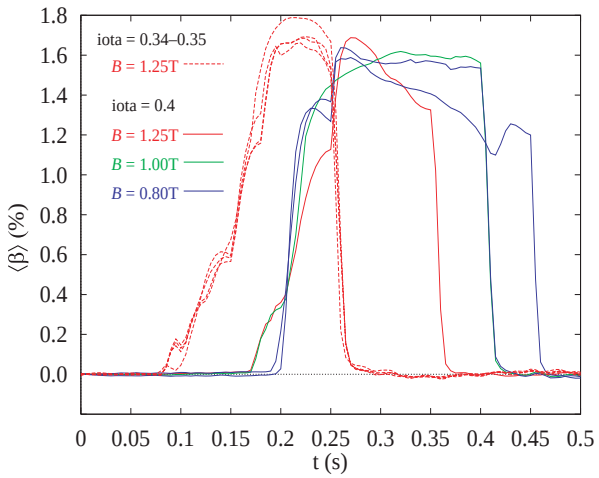


**Fig. 2.** Reconstructed time traces of ⟨β⟩ using DIAGNO calculated diamagnetic signals for discharges at differing experimental conditions. Central beta values of up to about 4% were reached.

### *Toroidal current effects*

On W7-AS, the usual operation is net current free, which means that the net toroidal plasma current is kept at zero by inductive compensation. However, the toroidal current ($I_{pl}$) within each flux surface does not vanish and thus alters the ι profile. A large-aspect-ratio estimate for the change in ι is given by

$$\Delta\iota(r_{eff}) = I_{pl}(r_{eff})R/\,[2\Phi(r_{eff})]$$

with $r_{eff}$ and $R$ the minor and major radii, respectively, and $\Phi$ the toroidal magnetic flux. For vanishing net current, the internal current density distribution usually has no influence on the flux surface geometry. Thus, to evaluate ι profiles in net-current-free discharges, it is sufficient to know the finite-beta changes on ι and then correct the profile using the toroidal current profile deduced from neoclassical theory and deposition profiles.

A stellarator-tokamak operation with internally or externally driven net toroidal currents is used to study the dependence of plasma confinement on ι and shear. For experimental details on such discharges see, e.g., *Stellarator News* 49. Figure 3 shows the variation in the ι profile and thus in the shear achieved in this way keeping the boundary ι value approximately constant. Net toroidal currents not only affect the ι-profile but also the flux surface geometry depending on the currents' magnitude and sign. Calculations show that the excursion of the flux surfaces in $R$ increases with positive net current (the shape tends to be more oblate) and decreases with negative net current (higher vertical elongation). Good agreement of the calculated flux surfaces in two cases with large toroidal currents (±30 kA at $B$ = 2.5 T, $\iota_{tot} \sim 0.4$) with the tomographically reconstructed soft X-ray emissivity measured by the new MiniSoX camera system [4] is shown in Fig. 4.

### *Discussion of NEMEC calculations*

Up to high beta and rather high currents, equilibrium calculations for W7-AS with NEMEC are in good agreement with the experiment. This gives confidence for W7-X, for which changes in the equilibrium due to finite-beta values are predicted to be much smaller because of the higher reduction of the average toroidal curvature and the higher operational range in ι ($\iota_{vac} \sim 1$).

Despite the good agreement with the experiment, there are limitations in the NEMEC applications. The assumption of nested flux surfaces excludes the detection of ergodic regions or islands. For this, more advanced equilibrium solvers, such as HINT or PIES, have to be applied. However, their computational requirements are orders of magnitude higher than those of NEMEC. Furthermore, the Fourier representation of the equilibrium quantities together with the energy minimization method applied limits the resolution of boundary structures, which require high Fourier harmonics and contain comparably small

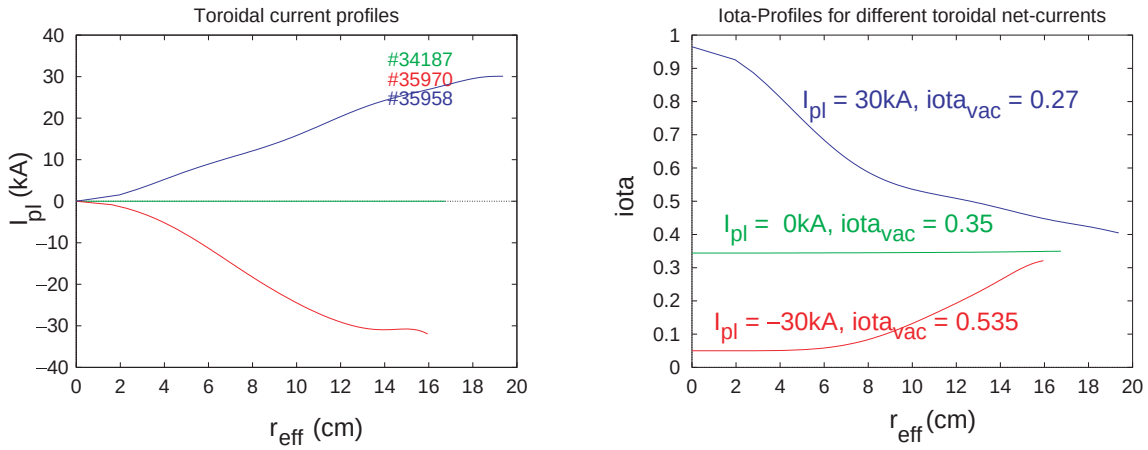


**Fig. 3.** Profiles of the toroidal net current and the resulting ι profiles. Different vacuum ι values have been chosen to reach approximately the same boundary ι value with the corresponding net currents.

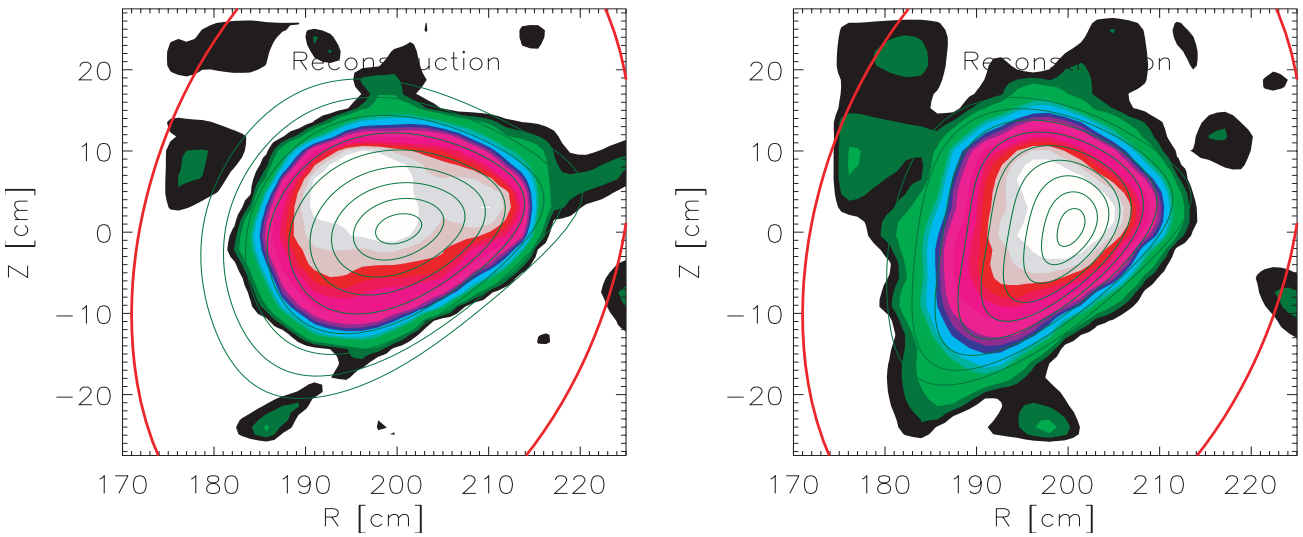


**Fig. 4.** Comparison of soft X-ray emissivity (MiniSoX system) with NEMEC flux surfaces for $I_{pl}$ = 30 kA (left) and $I_{pl}$ = –30 kA (right) shows good agreement in the gradient regions. A very flat central emission profile dominates the central contours for $I_{pl}$ = 30 kA. The outer structures are in the low-emissivity region and should be ignored.

energies. Such 5/*m* resonant structures have been seen by video observations of visible light. An example of the high-beta phase is shown in Fig. 5 for a discharge at $\iota_{vac}$ = 0.45. The boundary value of $\iota$ of a corresponding equilibrium calculation suggests *m* = 12 for the boundary structure. At lower $\iota$ values the indentation is smaller because of the higher *m* numbers of the resonances. Nevertheless, NEMEC shows a smooth plasma boundary without the actual indentation. Thus, care must be taken in the interpretation of data relating to the volume defined by the boundary.

These equilibrium calculations require orders of magnitude more CPU time than tokamak equilibrium calculations. For fast reconstructions accompanying an experiment on a shot-to-shot basis or even on line, NEMEC is not suitable with present-day computing power. Therefore, other approaches such as function parameterization must be explored and will be discussed in Part 2 of this article (next issue).

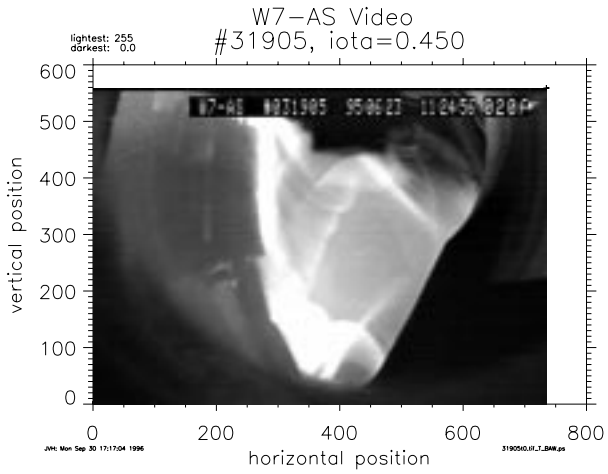


**Fig. 5.** Boundary structure seen by a video camera in visible light (C III). The structure may correspond to the 5/12 resonance.

J. Geiger, C. Goerner, J. V. Hofmann, R. Jaenicke, A. Weller
Max-Planck-Institut für Plasmaphysik
Euratom-IPP Association
85748 Garching, Germany

E-mail: geiger@ipp-garching.mpg.de

## References

[1] S. P. Hirshman, W. I. van Rij, and P. Merkel, Comput. Phys. Commun. **43** (1986) 143.

[2] H. Gardner, Nucl. Fusion **30** (1990) 1417.

[3] M. Kick et al., presented at the16th IAEA Conference on Plasma Physics and Controlled Nuclear Fusion Research, Montreal, 1996 (to be published in the proceedings).

[4] C. Goerner et al., presented at the 24th EPS Conference on Controlled Fusion and Plasma Physics, Berchtesgaden, 1997 (to be published in the proceedings).

# Collective Thomson scattering with 140-GHz gyrotrons at W7-AS

*Introduction*

Collective Thomson scattering (CTS) of electromagnetic radiation from thermal plasma fluctuations in principle allows measurement of the velocity distribution of plasma ions and their composition in the plasma. The use of powerful microwave radiation from gyrotrons opens new perspectives for the application of CTS, which is considered a promising candidate for alpha particle diagnostics in reactor-size tokamaks with deuterium-tritium (DT) operation.

We have performed initial experiments on W7-AS with different scattering geometries to demonstrate the applicability of gyrotrons for CTS. High-power gyrotrons developed for electron cyclotron resonance heating (ECRH) with power of a few hundred kilowatts and pulse durations of several seconds are well suited for application in CTS experiments. The millimeter wavelength range allows the use of a 90° scattering geometry with good spatial resolution of a few centimeters. Since on W7-AS ECRH usually provides plasma startup and operates at 70 and 140 GHz, the confining magnetic field is around 1.25 T (second cyclotron harmonic for 70 GHz) or 2.5 T (first harmonic for 70 GHz and second harmonic for 140 GHz). We have also investigated regimes with non-resonant field; in this case startup is achieved with a 900-MHz source, after which the plasma is sustained with neutral beam injection (NBI).

The CTS scattering experiments were performed with the probing microwave beam launched in two different toroidal sectors from the low magnetic field side. In both sectors the plasma column has an elliptical cross section with strong elongation in the vertical direction. In Sector I, a backscattering geometry was investigated; both the probing beam and receiving beam could be scanned together in the toroidal and poloidal directions. In Sector II, a nearly 90° scattering geometry was installed; this allowed us to measure the ion temperature with a spatial resolution of 4 cm. In this geometry only a poloidal scan remains accessible. These scattering arrangements are shown in Figs. 1 and 2; for details, see Ref. [1]. Typical plasma parameters in the experiments are densities $n_e$ between 0.2 and 1.2 × $10^{20}$ $m^{-3}$, electron temperatures $T_e$ between 0.5 and 2.0 keV, and ion temperatures $T_i$ between 0.2 and 0.7 keV.

*Thermal CTS spectra from backscattering*

For the backscattering geometry in Sector I, stray radiation turned out to be a major problem. Note that no beam dump is installed in W7-AS. In addition, to avoid the strong ECE background radiation, the CTS measurements were per-

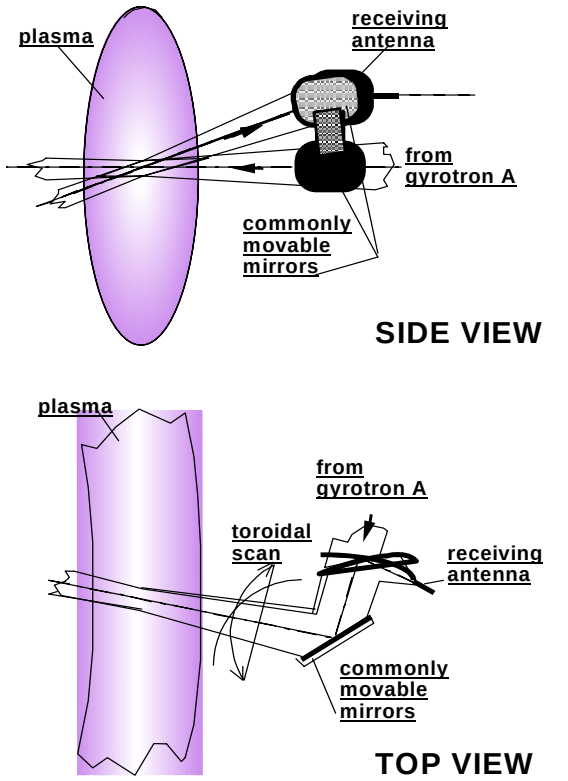


**Fig. 1.** Nearly backscattering geometry in Sector I. The rigidly connected emitting and receiving antennas are steerable in both toroidal and poloidal directions.

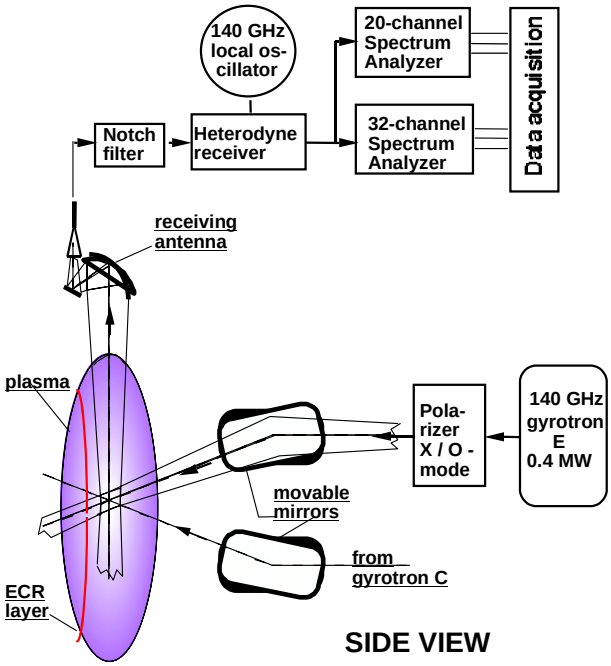


**Fig. 2.** Experimental set-up with nearly 90° scattering geometries in Sector II. Receiving antenna looking from the top in vertical direction is fixed; probing beams from gyrotrons C and E are movable in both the toroidal direction and half of the poloidal direction.

formed with a magnetic field of 1.25 T, which is the fourth harmonic for the probing frequency and is optically thin. However, this resulted in an enhanced level of stray radiation, practically none of which is absorbed by the plasma, a circumstance that also limited the pulse duration of the probing radiation to avoid damaging the vacuum vessel. Therefore, the pulse length was typically restricted to 50 ms.

The optimal position found for the launching-receiving antenna block minimized the stray radiation level at the receiving antenna input to less than 100 W. This corresponds to an antenna decoupling of up to 40 dB, which was low enough to allow measurements of thermal spectra. Thermal spectra were obtained from successive gyrotron shots, with and without plasma, by subtracting the background (shot without plasma). The signal level was found to increase with plasma density, as expected. The total bandwidth of the measured spectrum decreases with increasing density, which, together with the more than linear increase of the signal power, may be qualitatively explained by taking into account changes in the plasma refractive index [1].

Only a weak spatial resolution is provided in the backscattering geometry, and thus profile-averaged values of $n_e$ and $T_e$ were used for the theoretical modeling. For the CTS spectra taken at low density, a good fit to theoretical curves was obtained and good agreement of the CTS ion temperature with independent diagnostics is found.

### *Thermal CTS spectra from 90° scattering*

For the 90° scattering geometry in Sector II, the decoupling between emitting and receiving antennas is at least two orders of magnitude higher than in the backscattering geometry. This reduces the stray radiation to a very low level and allows measurement of the CTS spectra without any interference from the gyrotron noise.

To maintain the localized information from the CTS volume, the probing radiation should experience considerable absorption after its first pass through the scattering volume. This was achieved by launching the probing radiation in the X-mode and by placing the absorbing resonant layer off axis on the high-field side close to the inner chamber wall ($B_0$ = 2.35 T instead of $B_0$ = 2.5 T, which corresponds to absorption on axis). An example of a thermal CTS spectrum is shown in Fig. 3. The scattered signal (with the equivalent noise temperature of about 15 eV) is easily separated from the ECE background of about 50 eV. The spectrum of this background is flat with little deviation over a wide frequency range. The localization of the measurements was checked by toroidal scanning of the probing beam from the position of its optimal crossing with the receiving beam; as expected, the signal drops according to the angular width of the antenna radiation pattern, which corresponds to 4-cm spatial resolution.

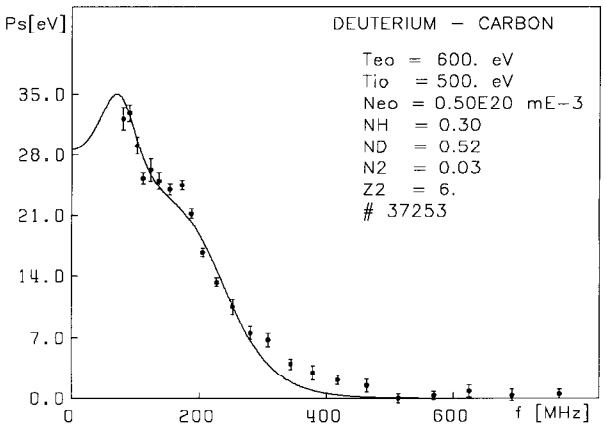


**Fig. 3.** CTS spectra from thermal density fluctuations obtained with 90° scattering.

The experimental CTS spectra are fitted well by theoretical curves for thermal density fluctuation spectra with the plasma parameters $n_e$ and $T_e$ taken from independent diagnostics; the plasma ion composition is fixed, and it is assumed that all ion components have equal temperatures. The values of the derived ion temperature are dependent on the H/D mixing ratio; naturally the value of ion temperature providing the best fit decreases with increasing hydrogen content. The fitting procedure is also sensitive to the amount of heavy impurities. The results show that good agreement for the value of $T_i$ can be obtained if the H/D mixing ratio is known.

### *Nonthermal CTS spectra from lower hybrid turbulence*

In the backscattering geometry (Sector I) a very intense narrow-band feature was detected in ECRH plasmas (X-mode, second harmonic) with a hydrogen neutral beam injected simultaneously for active charge-exchange (CX) diagnostics. Spectral measurements with a “zoom” spectral analyzer showed a relative bandwidth of about 2–3% of the mean frequency and a signal level up to a few million electron volts of equivalent noise temperature (see Fig. 4). This enhanced signal exists only in a very narrow angular range, which is comparable with the radiation pattern of the emitting and receiving antennas (1–2°) around the direction normal to the magnetic field. This intense scattered signal is certainly of nonthermal origin and is clearly correlated with repetitively pulsed neutral beam injection from the active CX diagnostic on W7-AS. From the frequency dependence on the density, the narrow-band feature was identified as being related to lower hybrid (LH) waves propagating almost transversely to the magnetic field. To explain the experimental findings, an instability mechanism for LH waves was proposed [2]; this occurs in the presence of a transverse ion beam under double resonance condition.

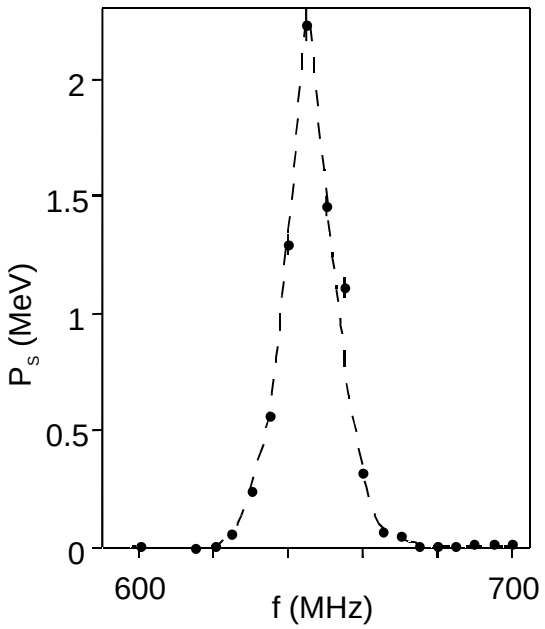


**Fig. 4.** Example of CTS spectrum from lower-hybrid turbulence excited by a transverse ion beam.

### *Conclusions*

CTS with gyrotrons as the sources of microwave probing radiation and heterodyne detection was investigated on W7-AS. The spectra of scattered radiation are characterized by high frequency resolution and small error bars. Backscattering and 90° scattering geometries were examined.

The thermal spectra in both scattering geometries were used to determine the ion temperature, yielding results in good agreement with independent diagnostics. The measurements performed in the 90° scattering geometry provide a spatial resolution of about 4 cm, which allows the measurement of radial ion temperature profiles even in a machine with the small dimensions of W7-AS. In reactor-scale installations, gyrotrons in the frequency range 140–200 GHz with long-pulse operation are attractive for alpha particle diagnostics. The present experiments can be regarded as providing proof of principle for this application.

### *Acknowledgment*

The work described in this article was performed by the Max Planck Institut für Plasmaphysik, Garching, Germany, the Institute of Applied Physics, Nizhni Novgorod, Russia, and the Institut für Plasmaforschung der Universität Stuttgart, Germany, with special support from the German Bundesministerium für Bildung, Wissenschaft, Forschung und Technologie.

V. Erckmann for the W7II-AS Team
IPP Garching, Germany, EURATOM Association,
in cooperation with
the Institute of Applied Physics, Russian Academy of Sciences, Nizhni Novgorod, Russia,
and the Institut für Plasmaforschung, Universität Stuttgart, Germany

E-mail: voe@ipp-garching.mpg.de

### References

[1] E. V. Suvorov et al., presented at the 24th EPS Conference on Controlled Fusion and Plasma Physics, Berchtesgaden, 1997 (to be published in the proceedings)

[2] E.V. Suvorov et al. Plasma Phys. Controlled Fusion **37** (1995) 1207.

# Evaluation of neoclassical transport in stellarators

Knowledge of the second adiabatic invariant $J_\parallel = \oint v_\parallel d\ell$ is useful for the analysis of stellarator confinement properties associated with trapped particles at low collisionality $\nu$ (long mean free path regime). The variation of $J_\parallel$ on a magnetic surface is directly related to the excursion $\delta r_n$ of a trapped particle across the magnetic surface during one bounce period $\tau_b$. This variation enters into the general equations of neoclassical transport theory for the contribution of the magnetic field asymmetry to the total particle and energy fluxes across magnetic surfaces (see, e.g., Refs. [1,2]).

Here we consider a method of computing this variation of $J_\parallel$ for an arbitrary magnetic field given in real-space coordinates. We also consider the use of these calculations in evaluating neoclassical transport fluxes for the $1/\nu$ transport regime. It is convenient to present the variation of $J_\parallel$ on a magnetic surface in the coordinate system $\psi$, $\theta_0$, $\phi$, where a magnetic field line is the intersection of the $\psi$ = const and $\theta_0$ = const surfaces and $\psi$ = const is the magnetic surface equation. Using the corresponding equations in Ref. [3] we can write

$$\frac{\partial J_\parallel}{\partial \theta_0} = \frac{eB}{mc}\sqrt{\frac{g}{g_{33}}}\delta\psi \,, \tag{1}$$

where $g_{jk}$ is the metric tensor of the coordinate system $\psi$, $\theta_0$, $\varphi$, $g$ = Det($g_{jk}$), and $\delta\psi$ is the increment in $\psi$ due to the excursion of a trapped particle across the magnetic surface during the bounce period. We compute $\delta\psi$ by the method of integration along magnetic field lines for a given stellarator magnetic field in Cartesian coordinates. For this calculation, guiding center drift equations are used in the limit of small gyroradius.

In the most perfect form (see, e.g., Ref. [4]) for arbitrary steady-state magnetic and electric fields, the guiding center drift equations can be written as

$$\frac{d\boldsymbol{r}}{dt} = \frac{\boldsymbol{B}}{B}v_\parallel + \boldsymbol{v}_d \,, \tag{2}$$

$$\boldsymbol{v}_d = \frac{c}{B^2 D}\left[\frac{m}{2eB}(2v_\parallel^2 + J_\perp B)(\boldsymbol{B}\times\nabla B + \boldsymbol{E}\times\boldsymbol{B})\right] + \frac{mcv_\parallel^2}{eB^4 D}\{\boldsymbol{B}\times[(\nabla\times\boldsymbol{B})\times\boldsymbol{B}]\} \,, \tag{3}$$

$$\frac{dv_\parallel}{dt} = \left(\frac{1}{2}J_\perp\nabla B - \frac{e}{m}\boldsymbol{E}\right)\cdot\frac{\boldsymbol{h} + \rho_\parallel\nabla\times\boldsymbol{h}}{D} \,, \tag{4}$$

where $\rho_\parallel = mcv_\parallel/(eB)$, $\boldsymbol{h} = \boldsymbol{B}/B$, $D = 1 + \rho_\parallel\boldsymbol{B}\cdot(\nabla\times\boldsymbol{B})/B^2$, and $J_\perp = v_\perp^2/B$ is the transverse adiabatic invariant.

We assume (as is common in calculating $J_\parallel$) that the Larmor radius of a particle and the electric field are rather small; consequently the displacement of a particle across a magnetic field line during one bounce period is insignificant. Therefore, as a first approximation, it is possible to neglect the second term on the right-hand side of Eq. (2) and to solve Eqs. (2) and (4) by integrating along a magnetic field line. Equation (3) is used in this case for calculating the rate of change of $\psi$, $d\psi/dt = \boldsymbol{v}_d\cdot\nabla\psi$, where for the $\nabla\psi$ calculation we use the method of Ref. [5]. As a result, we arrive at the set of equations containing Eq. (4) and the following equations:

$$\frac{d\boldsymbol{r}}{dt} = \boldsymbol{h}v_\parallel \,, \tag{5}$$

$$\frac{dP}{dt} = \frac{-v_\parallel}{B}\left(\frac{\partial B^1}{\partial\xi_1}P + \frac{\partial B^2}{\partial\xi_1}Q + \frac{\partial B^3}{\partial\xi_1}G\right) \,, \tag{6}$$

$$\frac{dQ}{dt} = \frac{-v_\parallel}{B}\left(\frac{\partial B^1}{\partial\xi_2}P + \frac{\partial B^2}{\partial\xi_2}Q + \frac{\partial B^3}{\partial\xi_2}G\right) \,, \tag{7}$$

$$\frac{dG}{dt} = \frac{-v_\parallel}{B}\left(\frac{\partial B^1}{\partial\xi_3}P + \frac{\partial B^2}{\partial\xi_3}Q + 3G\right) \,, \tag{8}$$

$$\frac{d\psi}{dt} = \boldsymbol{v}_d\cdot\nabla\psi \,. \tag{9}$$

In Eqs. (6)–(8), $B^j$ are the contravariant components of the vector in a normal curvilinear system of coordinates $\xi_j$, $P = \partial\psi/\partial\xi_1$, $Q = \partial\psi/\partial\xi_2$, $G = \partial\psi/\partial\xi_3$, and the multiplier $v_\parallel/B$ corresponds to the variable of integration $t$.

Calculating $\boldsymbol{r}$, $v_\parallel$, and $\nabla\psi$ with the help of Eqs. (4)–(8) and simultaneously solving Eq. (9), we find the value for each moment of time $t$. For $t = \tau_b$ we obtain

$$\delta\psi = \psi(\tau_b) \qquad [\psi(0) = 0] \,. \tag{10}$$

The initial conditions needed for solving Eqs. (4)–(9) can be determined from the preceding computation of the magnetic surface of interest. For a part of this surface corresponding to one magnetic field period, we select a row of magnetic field lines for which we wish to calculate $\delta\psi$. For each of these lines, the point corresponding to a minimum $B$ value is taken as the initial point of integration in Eqs. (4)–(9). The initial values of $\nabla\psi$ at these points are determined using the method of Ref. [5] concurrently with the magnetic surface computation. Solving Eqs.(4)–(9) under these initial conditions, one can obtain the $\delta\psi$ distribution as a function of the initial value of the particle longitudinal velocity $v_{\parallel j}$ and the position of the considered

segment of the magnetic field line on the magnetic surface (this position corresponds to a certain value of $\theta_0$).

The results of the $\delta\psi$ calculation (10) can be used to obtain $\partial J_\parallel/\partial\theta_0$ [with the help of Eq. (1)] as well as $\delta r_n$ and the normal to a magnetic surface component of the bounce-averaged velocity of the trapped particle drift $v_{an}$:

$$\delta r_n = \frac{\delta\psi}{|\nabla\psi_i|}, \quad v_{an} = \frac{\delta r_n}{\tau_b}, \tag{11}$$

where $\nabla\psi_i$ is the $\nabla\psi$ value at the initial point of integration.

The results of the $\partial J_\parallel/\partial\theta_0$ calculations can be directly used in evaluating the neoclassical fluxes associated with the magnetic field asymmetry for stellarators. Using Eqs. (2.1) and (2.2) of Ref. [6], where the variables $\xi_j$ correspond to the variables $\psi, \theta_0, \varphi$ in the present paper, one can obtain the equations for the particle and energy fluxes, $sF_n$ and $sF_T$, for the $1/\nu$ transport regime (across the magnetic surface for a magnetic field period):

$$sF_n = -\frac{c^2\pi}{\nu_j e_j^2 m_j}\int\frac{d\theta_0}{B}\sqrt{\frac{g_{33}}{g}}\int_0^\infty\frac{dJ_\perp}{A_j\nu^2}\frac{\partial f_j^{(0)}}{\partial\psi}$$

$$\times \int_{w_{min}}^{w_{max}}\frac{dw}{J_\parallel(w)}\left[\int_{w_{min}}^{w} dw'\frac{\partial J_\parallel}{\partial\theta_0}\right]^2. \tag{12}$$

Here $f_j^{(0)}$ is the Maxwellian distribution for $j$-type particles, $w$ is the particle energy, and $w_{min} = w_{min}(J_\perp, \psi, \theta_0)$ and $w_{max} = w_{max}(J_\perp, \psi, \theta_0)$ are the minimum and maximum energies which are possible for the trapped particles. The Coulomb frequency $\nu_j$ and the quantity $A_j$ are the same as in Refs. [1] and [6]. Since $\nu^2 \approx v_\perp^2 = J_\perp B \approx J_\perp B_0$, the derivative $\partial f_j^{(0)}/\partial\psi$ is taken out of the integrand for the integration over $w$. Here, $B_0$ is the average longitudinal magnetic field. The energy flux $sF_T$ differs from Eq. (12) by the factor $mJ_\perp B_0/2$ in the integrand.

To calculate the right-hand side of Eq. (12), it is also necessary to calculate $J_\parallel$ and to identify a method of integration over $\theta_0$. Equations (4)–(8) may be supplemented by the equation $dJ_\parallel(t)/dt = v_\parallel^2 [J_\parallel(0) = 0]$. Integration of this equation for the period $t = \tau_b$ gives the $J_\parallel$ value. The variable $\theta_0$ can be defined in such a way that $B\sqrt{g/g_{33}} = 1$ and $d\theta_0 = (\boldsymbol{B}\cdot\nabla\varphi)(d\ell_p/|\nabla\varphi\times\nabla\psi|)$. Here $\ell_p$ is an arc length of the curve that is the intersection of the magnetic surface and the $\varphi$ = const surface. With the use of these relationships the neoclassical transport fluxes, $sF_n$ and $sF_T$, can be calculated if $\partial J_\parallel/\partial\theta_0$ and $J_\parallel$ are obtained as functions of $J_\perp$ and $w$ (or $J_\perp$ and $v_{\parallel i}$).

To demonstrate the proposed technique let us consider a magnetic configuration that is one of possible real-space realizations of a zero-beta variant of quasihelical symmetry examined in magnetic coordinates in Ref. [7]. We consider the corresponding magnetic field as a superposition of toroidal harmonic functions containing the associated Legendre functions. The number of decomposition terms used is limited by the conditions $0 \le n \le 12$, $m = m_p M$, $|M| \le 12$, where $n$ and $m$ are the poloidal and toroidal harmonic numbers and $m_p$ is the number of periods along the torus ($m_p = 6$). The results of the $v_{an}$ calculations performed with the help of Eqs. (10) and (11) show that for the near-boundary magnetic surface in the magnetic field under consideration, the maximum value of the quantity $\eta = v_{an}R/v_{\perp 0}r_{L0}$ turns out to be small ($v_{\perp 0} = \sqrt{J_\perp B_0}$, $r_{L0} = mcv_{\perp 0}/eB_0$ is the Larmor radius calculated for $B = B_0$, and $R$ is the major radius of the torus). On the average, this maximum value is approximately equal to $\eta_{max} \approx 0.05$ (note that for a standard stellarator model [1] $\eta_{max} \approx 0.5$).

This result is different from the results of similar calculations in Ref. [8], where the same configuration was considered and where $\eta_{max} \approx 0.25$ was obtained. This difference is explained as follows. In Ref. [8] the quantity $\delta r_n$ is a result of integration over $t$ for the normal to a magnetic surface component of the particle drift velocity. In general, this integration does not give the true value of the particle excursion across a magnetic surface; the equations of Ref. [8] are valid for the $v_{an}$ calculations only for small variation of the magnitude of $\nabla\psi$ within the particle trajectory (e.g., for deeply trapped particles). In the general case, for the $v_{an}$ calculations the equations presented here must be used.

It follows from Eq. (12) that the neoclassical transport coefficients are qualitatively proportional to the square of $\partial J_\parallel/\partial\theta_0$ [or to a square of $\eta$, as can be seen from Eqs. (1), (10), and (11)]. The maximum value of $\eta$ for the near-boundary magnetic surface is approximately a factor of ten less than $\eta_{max}$ for the standard stellarator model. Thus, for this surface one would expect that the contribution of the magnetic field asymmetry to the neoclassical transport coefficients would be a hundred times less than the corresponding contribution for the standard model of a stellarator [1] of equivalent size.

V. V. Nemov
Institute of Plasma Physics, National Science Center
Kharkov Institute of Physics and Technology
Kharkov 310108, Ukraine

**References**

[1] A. A. Galeev and R. Z. Sagdeev, p. 205 in Voprosy Teorii Plazmy (Problems of Plasma Theory), Vol. 7, Atomizdat, Moscow (1973).

[2] L. M. Kovrizhnykh, Nucl. Fusion **24** (1984) 851.

[3] B. B. Kadomtsev, in Plasma Physics and Problems of Controlled Thermonuclear Reactors, Vol. 3, Pergamon Press, New York, 1958; A. I. Morozov and L. S. Solov'ev, p. 177 in Voprosy Teorii Plazmy (Problems of Plasma Theory), Vol. 2, Gosatomizdat, Moscow (1963).

[4] T. G. Northrop and J. A. Rome, Phys. Fluids **21** (1978) 384; R. B. White, A. H. Boozer, and R. Hay, Phys. Fluids **25** (1982) 575; R. Littlejohn, J. Plasma Phys. **29** (1983) 111.

[5] V. V. Nemov, Nucl. Fusion **28** (1988) 1727.

[6] V. V. Nemov. Nucl. Fusion **17** (1977) 101.

[7] J. Nührenberg and R. Zille. Phys.Lett. A **129** (1988) 113.

[8] V. V. Nemov, "Average drift velocity of trapped particles in stellarators," p. 4 in *Stellarator News*, Issue 49 (Ed. J. A. Rome), January 1997.


# Jeffrey Harris moves to ANU

Since February 1997 Dr. Jeffrey H. Harris has been at the Australian National University (ANU) as professor, head of the Plasma Research Laboratory, and director of the National Plasma Fusion Research Facility. The experiment, now called H-1NF (National Facility), is a 3 field period flexible heliac with $R$ = 1 m and $a$ = 15 cm. H-1NF won US $6.5 million of additional capital funding in a competition in 1995–96, and a contract between the government and the ANU, signed in May 1997, and will run 5 years. The new funding will pay for an upgrade of the magnetic field to 1 T and an increase in heating power to 500–1000 kW. The National Institute of Fusion Science (NIFS) and Kyoto University in Japan have acted together to lend H-1NF a 200-kW, 28-GHz gyrotron and power supply, which have been installed and tested. The next big step is the acquisition of a new magnet power supply, for which a tender offer will soon be issued.

Collaborative activities with a number of Australian universities in the area of diagnostics are under way, under the aegis of the Australian Fusion Research Group, which is affiliated with the Australian Institute of Nuclear Science and Engineering. Additional collaborations with overseas laboratories are being negotiated, with agreements already signed with NIFS and Kyoto University.

The Plasma Research Laboratory at the ANU has a staff of about 20, plus students, and conducts research in basic plasma physics, space physics, and plasma processing of materials, in addition to work on toroidal confinement for fusion.